universe

IMPACT FACTOR 2.813

CITESCORE 3.2

Article

On the $\eta_1(1855)$, $\pi_1(1400)$ and $\pi_1(1600)$ as Dynamically Generated States and Their SU(3) Partners

Mao-Jun Yan, Jorgivan M. Dias, Adolfo Guevara, Feng-Kun Guo and Bing-Song Zou

MDPI

https://doi.org/10.3390/universe9020109

universe

MDPI

Article

On the $\eta_1(1855)$, $\pi_1(1400)$ and $\pi_1(1600)$ as Dynamically Generated States and Their SU(3) Partners

Mao-Jun Yan [1,*], Jorgivan M. Dias [1], Adolfo Guevara [1], Feng-Kun Guo [1,2,3,*] and Bing-Song Zou [1,2,4]

[1] CAS Key Laboratory of Theoretical Physics, Institute of Theoretical Physics, Chinese Academy of Sciences, Beijing 100190, China
[2] School of Physical Sciences, University of Chinese Academy of Sciences, Beijing 100049, China
[3] Institute of Modern Physics, Chinese Academy of Sciences, Lanzhou 730000, China
[4] Peng Huanwu Collaborative Center for Research and Education, Beihang University, Beijing 100191, China
* Correspondence: yanmaojun@itp.ac.cn (M.-J.Y.); fkguo@itp.ac.cn (F.-K.G.)

Abstract: In this work, we interpret the newly observed $\eta_1(1855)$ resonance with exotic $J^{PC} = 1^{-+}$ quantum numbers in the $I = 0$ sector, reported by the BESIII Collaboration, as a dynamically generated state from the interaction between the lightest pseudoscalar mesons and axial-vector mesons. The interaction is derived from the lowest order chiral Lagrangian from which the Weinberg–Tomozawa term is obtained, describing the transition amplitudes among the relevant channels, which are then unitarized using the Bethe–Salpeter equation, according to the chiral unitary approach. We evaluate the $\eta_1(1855)$ decays into the $\eta\eta'$ and $K\bar{K}^*\pi$ channels and find that the latter has a larger branching fraction. We also investigate its SU(3) partners, and according to our findings, the $\pi_1(1400)$ and $\pi_1(1600)$ structures may correspond to dynamically generated states, with the former one coupled mostly to the $b_1\pi$ component and the latter one coupled to the $K_1(1270)\bar{K}$ channel. In particular, our result for the ratio $\Gamma(\pi_1(1600) \to f_1(1285)\pi)/\Gamma(\pi_1(1600) \to \eta'\pi)$ is consistent with the measured value, which supports our interpretation for the higher π_1 state. We also report two poles with a mass about 1.7 GeV in the $I = 1/2$ sector, which may be responsible for the $K^*(1680)$. We suggest searching for two additional η_1 exotic mesons with masses around 1.4 and 1.7 GeV. In particular, the predicted $\eta_1(1700)$ is expected to have a width around 0.1 GeV and can decay easily into $K\bar{K}\pi\pi$.

Keywords: hadronic molecule; $\eta_1(1855)$; $\pi_1(1400)$; $\pi_1(1600)$

Citation: Yan, M.-J.; Dias, J.M.; Guevara, A.; Guo, F.-K.; Zou, B.-S. On the $\eta_1(1855)$, $\pi_1(1400)$ and $\pi_1(1600)$ as Dynamically Generated States and Their SU(3) Partners. *Universe* **2023**, *9*, 109. https://doi.org/10.3390/universe9020109

Academic Editor: Maria Vasileiou

Received: 16 January 2023
Revised: 16 February 2023
Accepted: 17 February 2023
Published: 19 February 2023

1. Introduction

Over the last two decades, the experimental observation of many new hadronic states is challenging our current understanding of hadrons as conventional mesons and baryons with valence contents of quark–antiquark and three quarks, respectively, since most of them do not fit in the well-known quark model. This difficulty brought back a long-standing discussion on the exotic hadronic structures, i.e., multiquark configurations that might have quantum numbers beyond those assigned to the conventional mesons and baryons [1,2].

Exotic quark configurations, such as tetraquarks [3,4], hadron–hadron molecules [5], glueballs, and hybrids [6,7], among others, have been suggested to describe suitably most of the properties of these new states, such as the J^{PC} quantum numbers, mass, and decay width, especially for those lying in the charmonium and bottomonium spectra.

On the other hand, distinguishing the exotic states from the conventional hadrons is a more complicated task in the light quark sector. Many states have their masses close to each other, and the possibility of mixing brings additional difficulty to the problem. The situation improves as the quantum numbers do not fall into those allowed by the conventional quark model. It seems to be the case of the newly discovered state, dubbed $\eta_1(1855)$, by the BESIII Collaboration [8,9], observed in the invariant mass distribution of the $\eta\,\eta'$ meson pair in the $J/\psi \to \gamma\,\eta\,\eta'$ decay channel with a significance of 19σ. Its

mass and width reported by BESIII are $1855 \pm 9^{+6}_{-1}$ MeV and $188 \pm 18^{+3}_{-8}$ MeV, respectively, with likely $J^{PC} = 1^{-+}$ quantum numbers, which cannot be formed by a pair of quark and antiquark. The $\eta_1(1855)$ is not the only state experimentally found with that set of quantum numbers. As of today, three other hadronic structures, called $\pi_1(1400)$, $\pi_1(1600)$, and $\pi_1(2015)$, with $J^{PC} = 1^{-+}$, were observed by several collaborations [7,10].

From the theoretical point of view, the hybrid model has been used to investigate these exotic meson states, in particular the 1^{-+} ones. Lattice quantum chromodynamics (QCD) calculations have pointed out hybrid supermultiplets with exotic J^{PC} quantum numbers, including the 1^{-+} one [11–16]. In this picture, however, the mass of the lightest 1^{-+} state and decay modes are inconsistent with the corresponding experimental results, while the $\pi_1(1600)$ and $\pi_1(2015)$ structures can fit into the nonets predicted by lattice QCD [7].

The newly observed $\eta_1(1855)$ state has also been the focus of some studies. In particular, the authors in Ref. [17] proposed two hybrid nonet schemes in which the $\eta_1(1855)$ resonance can be either the lower or higher mass state with isospin $I = 0$. In Ref. [18], an effective Lagrangian respecting flavor, parity, and charge conjugation symmetries is used to study the hybrid nonet decays into two-body meson states. The authors have fixed the couplings to those two-body meson states by performing a combined fit to the experimental and lattice results available. As a result, the decay width value estimated for the isoscalar member of the hybrid nonet agrees with the one observed for $\eta_1(1855)$ state. Additionally, addressing the same picture, Ref. [19] applied the approach of QCD sum rules to describe the $\eta_1(1855)$ mass. By contrast, within the same approach, the $\eta_1(1855)$ resonance is described as a tetraquark state in Ref. [20].

The $\eta_1(1855)$ resonance also supports a meson–meson molecule interpretation due to its proximity to the $K\bar{K}_1(1400)$ threshold, as put forward by Refs. [21,22]. In particular, the authors in Ref. [21] have investigated the $K\bar{K}_1(1400)$ interaction through the one-boson exchange model. According to their findings, the $K\bar{K}_1(1400)$ system binds for cut-off values above 2 GeV with a monopole form factor. In addition, the comparison between their result for the branching fraction $\mathcal{B}(\eta_1 \to \eta\,\eta')$ to the experimental one led them to conclude that the $K\bar{K}_1(1400)$ molecule can explain the $\eta_1(1855)$ structure.

An important point to be addressed is the meson–meson interaction around the $K_1(1400)\bar{K}$ threshold for the $J^{PC} = 1^{-+}$ quantum numbers. In this sector, many meson–meson pairs may contribute to that interaction, so a coupled-channel treatment seems appropriate to take these contributions into account. In particular, hadron–hadron interactions in coupled channels have been studied in many works to describe the properties of the new hadronic systems experimentally observed. In those cases, these hadronic structures are called dynamically generated states.

Following this approach, in this work, we aim to explore the $\eta_1(1855)$, $\pi_1(1400)$, and $\pi_1(1600)$ hadronic systems as dynamically generated states from pseudoscalar-axial vector meson interactions in coupled channels. Specifically, the low-energy interactions are given by the Weinberg–Tomozawa (WT) term from chiral Lagrangians at the leading order of the chiral expansion by treating the axial vector mesons as matter fields and the pseudoscalar mesons as the pseudo-Nambu–Goldstone bosons of the spontaneous breaking of chiral symmetry. Such Lagrangians have been used to study many hadron structures stemming from meson–meson and meson–baryon interactions in coupled channels in light and heavy sectors, see, e.g., Refs. [23–27]. In our case, the amplitudes obtained from the WT term are unitarized via the Bethe–Salpeter equation from which bound states/resonances manifest as poles in the physical/unphysical Riemann sheets of the scattering matrices. The existence of a whole family of kaonic bound states has been pointed out in Ref. [28] based on unitarizing the WT term for the scattering of the kaon off isospin-1/2 matter fields taking heavy mesons and doubly-charmed baryons as examples. As we shall show in this work, the newly observed $\eta_1(1855)$ structure may correspond to a dynamically generated state from the pseudoscalar-axial vector interaction in the isospin $I = 0$ sector coupling strongly to the $K_1(1400)\bar{K}$ channel. Moreover, the $\pi_1(1400)$ and $\pi_1(1600)$, may be assigned as the $\eta_1(1855)$ SU(3) partners which are also dynamically generated from the pseudoscalar-axial

vector meson interactions in the $I = 1$ sector. The former resonance couples mainly to the $b_1\pi$ channel, and the latter has the $K_1(1270)\bar{K}$ as its main coupled channel.

In addition, we have also found two poles around 1.7 GeV in the $I = 1/2$ sector. These poles are particularly interesting as they could be the origin of the $K^*(1680)$ structure observed experimentally [10], which is the main component of the 1^- contribution to the ϕK mass distribution in the $B \to J/\psi\phi K$ decays recently measured by LHCb [29].

This paper is organized as follows. In Section 2, we discuss the relevant channels contributing to the pseudoscalar-axial vector meson interactions and the use of the chiral unitary approach (ChUA) for the evaluation of the transition amplitudes among those channels. In Sections 3 and 4, we investigate the dynamical generation of poles stemming from those interactions in the $I = 0$ and $I = 1$ sectors and discuss their possible decay channels. Finally, in Section 5, we also explore the dynamical generation of poles for $I = 1/2$ and their connection to the vector $K^*(1680)$ structure observed experimentally. Section 6 gives a summary.

2. Coupled Channel Scattering In Chiral Unitary Approach

We investigate the interactions between axial and pseudoscalar mesons in coupled channels in the $1300 \sim 2000$ MeV energy range. First, we need to determine the space of states contributing to the interaction in this energy range.

In Tables 1–4, we list all the relevant channels for the problem under consideration along with their corresponding mass thresholds. The channels are organized from the lower to higher mass values and by the isospin, 0, 1, and 1/2, respectively.

Table 1. $J^{PC} = 1^{-+}$ meson-meson channels with $I = 0$. The threshold masses are in the units of MeV.

Channel	$a_1\pi$	$K_1(1270)\bar{K}$	$f_1(1285)\eta$	$K_1(1400)\bar{K}$	$f_1(1420)\eta$
Threshold	1368	1748	1829	1898	1973

Table 2. $J^{PC} = 1^{-+}$ meson–meson channels with $I = 1$. The threshold masses are in the units of MeV.

Channel	$b_1\pi$	$f_1(1285)\pi$	$f_1(1420)\pi$	$K_1(1270)\bar{K}$	$a_1\eta$	$K_1(1400)\bar{K}$
Threshold	1367	1419	1564	1748	1777	1895

Table 3. $J^P = 1^-$ meson–meson channels with $I = 1/2$. The threshold masses are in the units of MeV. Here the flavor-neutral axial vector mesons have $J^{PC} = 1^{++}$.

Channel	a_1K	$f_1(1285)K$	$K_1(1270)\eta$	$f_1(1420)K$	$K_1(1400)\eta$
Threshold	1725	1777	1800	1921	1947

Table 4. $J^P = 1^-$ meson–meson channels with $I = 1/2$. The threshold masses are in the units of MeV. Here, the flavor-neutral axial vector mesons have $J^{PC} = 1^{+-}$.

Channel	$h_1(1170)K$	b_1K	$K_1(1270)\eta$	$h_1(1415)K$	$K_1(1400)\eta$
Threshold	1661	1725	1800	1911	1947

In what follows, we shall discuss the relevant scattering amplitudes among all those channels above for each isospin sector. These transitions can be written in the form of the WT term which then is unitarized. Notice that the channels displayed in Tables 3 and 4, in principle, should be grouped in the same space of states since they share identical isospin and J^P quantum numbers. However, the relevant transitions among them arise only at the next-to-leading order in the chiral expansion; see the discussion around Equation (17) below. Thus, such transitions are of higher order than that of the WT term and will be neglected here.

2.1. The Weinberg–Tomozawa Term

In order to study the interactions among all the channels listed in the previous tables, we have to evaluate the interactions between the pseudoscalar and axial-vector mesons. The latter are organized in two SU(3) octets according to their J^{PC} quantum numbers.

$$A_1 = \begin{pmatrix} \frac{a_1^0}{\sqrt{2}} + \frac{f_1^8}{\sqrt{6}} & a_1^+ & K_{1A}^+ \\ a_1^- & -\frac{a_1^0}{\sqrt{2}} + \frac{f_1^8}{\sqrt{6}} & K_{1A}^0 \\ K_{1A}^- & \bar{K}_{1A}^0 & -\frac{2f_1^8}{\sqrt{6}} \end{pmatrix} \tag{1}$$

is the octet of resonances of axial-vector states with $J^{PC} = 1^{++}$ for the flavor-neutral mesons, and

$$B_1 = \begin{pmatrix} \frac{b_1^0}{\sqrt{2}} + \frac{h_1^8}{\sqrt{6}} & b_1^+ & K_{1B}^+ \\ b_1^- & -\frac{b_1^0}{\sqrt{2}} + \frac{h_1^8}{\sqrt{6}} & K_{1B}^0 \\ K_{1B}^- & K_{1B}^0 & -\frac{2}{\sqrt{6}} h_1^8 \end{pmatrix} \tag{2}$$

describes the octet of axial-vector resonances with $J^{PC} = 1^{+-}$. The singlet and $I = 0$ octet flavor eigenstates are not mass eigenstates; that is, the pairs of $f_1(1420)$, $h_1(1415)$ (also known as $h_1(1380)$) and $f_1(1285)$, $h_1(1170)$ mesons are mixtures of the singlet $(^1)$ and octet $(^8)$ mesons, such that

$$\begin{pmatrix} |f_1(1285)\rangle \\ |f_1(1420)\rangle \end{pmatrix} = \begin{pmatrix} \cos\theta_{^3P_1} & \sin\theta_{^3P_1} \\ -\sin\theta_{^3P_1} & \cos\theta_{^3P_1} \end{pmatrix} \begin{pmatrix} |f_1^1\rangle \\ |f_1^8\rangle \end{pmatrix}, \tag{3}$$

and

$$\begin{pmatrix} |h_1(1170)\rangle \\ |h_1(1415)\rangle \end{pmatrix} = \begin{pmatrix} \cos\theta_{^1P_1} & \sin\theta_{^1P_1} \\ -\sin\theta_{^1P_1} & \cos\theta_{^1P_1} \end{pmatrix} \begin{pmatrix} |h_1^1\rangle \\ |h_1^8\rangle \end{pmatrix}. \tag{4}$$

Furthermore, the K_{1A} and K_{1B} members of the multiplets in Equations (1) and (2) are the strange partners of the $a_1(1260)$ and $b_1(1235)$, and their mixture contributes to the physical $K_1(1270)$ and $K_1(1400)$ mesons, that is

$$\begin{pmatrix} |K_1(1270)\rangle \\ |K_1(1400)\rangle \end{pmatrix} = \begin{pmatrix} \sin\theta_{K_1} & \cos\theta_{K_1} \\ \cos\theta_{K_1} & -\sin\theta_{K_1} \end{pmatrix} \begin{pmatrix} |K_{1A}\rangle \\ |K_{1B}\rangle \end{pmatrix}. \tag{5}$$

The corresponding values for the mixing angles in Equations (3)–(5) are listed in Table 5, where they are grouped into two sets, denoted by A and B. Although set B is preferred in Ref. [30], we will use both sets to have an estimate of the uncertainties caused by such an angle.

Table 5. Two sets of values of the axial-vector meson mixing angles taken from Ref. [30]. Set B is preferred in Ref. [30]. The η-η' mixing angle θ_P is taken from Ref. [31]. For more discussions about these mixing angles, we refer to the review of *Quark Model* in the *Review of Particle Physics* [10].

Angles	θ_{K_1}	$\theta_{^3P_1}$	$\theta_{^1P_1}$	θ_P
Set A	57°	52°	−17.5°	−17°
Set B	34°	23.1°	28.0°	−17°

In order to determine the WT term we start with the Lagrangian (see, e.g., Ref. [32])

$$\mathcal{L}_0 = -\frac{1}{4}\left\langle V_{\mu\nu}V^{\mu\nu} - 2M_V^2 V_\mu V^\mu \right\rangle, \tag{6}$$

where $\langle , \rangle$ takes trace in the SU(3) flavor space,

$$V_{\mu\nu} = \mathcal{D}_\mu V_\nu - \mathcal{D}_\nu V_\mu \,, \tag{7}$$

while $\mathcal{D}_\mu$ is the chirally covariant derivative, which when acting on SU(3) octet matter fields reads as

$$\mathcal{D}_\mu = \partial_\mu + \left[\Gamma_\mu, \right], \tag{8}$$

with $[\ ,\ ]$ the usual commutator. In addition, Γ_μ stands for the chiral connection, given by

$$\Gamma_\mu = \frac{1}{2}\left(u^\dagger \partial_\mu u + u \partial_\mu u^\dagger\right), \tag{9}$$

with

$$u = \exp\left(\frac{i}{\sqrt{2}F_\pi}\phi^8\right), \tag{10}$$

where $F_\pi = 92.1$ MeV is the pion decay constant [10], and ϕ^8 is the pseudoscalar SU(3) octet, that is

$$\phi^8 = \begin{pmatrix} \frac{\pi^0}{\sqrt{2}} + \frac{1}{\sqrt{6}}\eta_8 & \pi^+ & K^+ \\ \pi^- & -\frac{1}{\sqrt{2}}\pi^0 + \frac{1}{\sqrt{6}}\eta_8 & K^0 \\ K^- & \bar{K}^0 & -\frac{2}{\sqrt{6}}\eta_8 \end{pmatrix}. \tag{11}$$

In addition, the physical η and η' mesons are the mixtures of η^8 and η^1

$$\begin{pmatrix} |\eta\rangle \\ |\eta'\rangle \end{pmatrix} = \begin{pmatrix} -\sin\theta_P & \cos\theta_P \\ \cos\theta_P & \sin\theta_P \end{pmatrix} \begin{pmatrix} |\eta^1\rangle \\ |\eta^8\rangle \end{pmatrix}, \tag{12}$$

where η^1 becomes the ninth pseudo-Goldstone boson in large N_c QCD [33–36]. The Goldstone boson nonet is written as

$$\phi^9 \quad = \quad \phi^8 + \frac{1}{\sqrt{3}}\eta^1, \tag{13}$$

which leads to a relation in the commutator

$$\left[\phi^9, \partial_\mu \phi^9\right] \quad = \quad \left[\phi^8, \partial_\mu \phi^8\right]. \tag{14}$$

Therefore, only the scattering of the octet Goldstone bosons off the axial-vector mesons in Weinberg–Tomozawa term contributes to $J^{P(C)} = 1^{-(+)}$ spectrum.

The covariant derivative $\mathcal{D}_\mu$ by means of the connection Γ_μ encodes the leading order interaction between the pseudoscalar mesons and the vector field V_μ [32,37,38]. Therefore, by replacing the V_μ field to the axial-vector field A_μ corresponding to either the A_1 or B_1 multiplet, the chiral transition between ϕ^8 (pseudoscalar) and $A(1^+)$ (axial-vector) is described by the following interaction Lagrangian

$$\mathcal{L}_I = -\frac{1}{4F_\pi^2}\left\langle \left[A^\mu, \partial^\nu A_\mu\right]\left[\phi^8, \partial_\nu \phi^8\right]\right\rangle, \tag{15}$$

which accounts for the WT interaction term for the $PA \to PA$ process, with P and A corresponding to the pseudoscalar and axial-vector mesons, respectively. From this Lagrangian we obtain the S-wave transition amplitude among the channels listed in Tables 1–4, that is

$$V_{ij}(s) = -\frac{\epsilon\cdot\epsilon'}{8F_\pi^2}C_{ij}\left[3s - \left(M^2 + m^2 + M'^2 + m'^2\right) - \frac{1}{s}\left(M^2 - m^2\right)\left(M'^2 - m'^2\right)\right], \tag{16}$$

where $\epsilon(\epsilon')$ stands for the polarization four-vector of the incoming (outgoing) axial-vector meson [25,39]. The masses $M(M'), m(m')$ correspond to the initial (final) axial-vector mesons and initial (final) pseudoscalar mesons, respectively. The indices i and j represent the initial and final PA states, respectively. The coefficients C_{ij} are given in Tables 6–9.

Table 6. C_{ij} coefficients in Equation (16) for axial and pseudoscalar pairs coupled to $J^{PC} = 1^{-+}$ in S-wave and $I = 0$.

C_{ij}	$a_1\pi$	$K_1(1270)\bar{K}$	$f_1(1285)\eta$	$K_1(1400)\bar{K}$	$f_1(1420)\eta$
$a_1\pi$	-4	$\sqrt{\frac{3}{2}}\sin\theta_{K_1}$	0	$\sqrt{\frac{3}{2}}\cos\theta_{K_1}$	0
$K_1(1270)\bar{K}$		-3	$-\frac{3}{\sqrt{2}}\sin\theta_{^3P_1}\sin\theta_{K_1}$	0	$-\frac{3}{\sqrt{2}}\cos\theta_{^3P_1}\sin\theta_{K_1}$
$f_1(1285)\eta$			0	$-\frac{3}{\sqrt{2}}\cos\theta_{K_1}\sin\theta_{^3P_1}$	0
$K_1(1400)\bar{K}$				-3	$-\frac{3}{\sqrt{2}}\cos\theta_{^3P_1}\cos\theta_{K_1}$
$f_1(1420)\eta$					0

Table 7. C_{ij} coefficients in Equation (16) for axial and pseudoscalar pairs coupled to $J^{PC} = 1^{-+}$ in S-wave and $I = 1$.

C_{ij}	$b_1\pi$	$f_1(1285)\pi$	$f_1(1420)\pi$	$K_1(1270)\bar{K}$	$a_1\eta$	$K1(1400)\bar{K}$
$b_1\pi$	-2	0	0	$\cos\theta_{K_1}$	0	$-\sin\theta_{K_1}$
$f_1(1285)\pi$		0	0	$\sqrt{\frac{3}{2}}\sin\theta_{K_1}\sin\theta_{^3P_1}$	0	$\sqrt{\frac{3}{2}}\cos\theta_{K_1}\sin\theta_{^3P_1}$
$f_1(1420)\pi$			0	$\sqrt{\frac{3}{2}}\cos\theta_{^3P_1}\sin\theta_{K_1}$	0	$\sqrt{\frac{3}{2}}\cos\theta_{K_1}\cos\theta_{^3P_1}$
$K_1(1270)\bar{K}$				-1	$-\sqrt{\frac{3}{2}}\sin\theta_{K_1}$	0
$a_1\eta$					0	$-\sqrt{\frac{3}{2}}\cos\theta_{K_1}$
$K_1(1400)\bar{K}$						-1

Table 8. C_{ij} coefficients in Equation (16) for axial and pseudoscalar pairs coupled to $J^P = 1^-$ in S-wave and $I = 1/2$. Here the flavor-neutral axial mesons have $J^{PC} = 1^{++}$.

C_{ij}	a_1K	$f_1(1285)K$	$K_1(1270)\eta$	$f_1(1420)K$	$K_1(1400)\eta$
a_1K	-2	0	$-\frac{3}{2}\sin\theta_{K_1}$	0	$-\frac{3}{2}\cos\theta_{K_1}$
$f_1(1285)K$		0	$\frac{3}{2}\sin\theta_{K_1}\sin\theta_{^3P_1}$	0	$\frac{3}{2}\sin\theta_{K_1}\cos\theta_{K_1}$
$K_1(1270)\eta$			0	$\frac{3}{2}\cos\theta_{^3P_1}\sin\theta_{K_1}$	0
$f_1(1420)K$				0	$\frac{3}{2}\cos\theta_{^3P_1}\cos\theta_{K_1}$
$K_1(1400)\eta$					0

Table 9. C_{ij} coefficients in Equation (16) for axial and pseudoscalar pairs coupled to $J^P = 1^-$ in S-wave and $I = 1/2$. Here the flavor-neutral axial mesons have $J^{PC} = 1^{+-}$.

C_{ij}	$h_1(1170)K$	b_1K	$K_1(1270)\eta$	$h_1(1415)K$	$K_1(1400)\eta$
$h_1(1170)K$	0	0	$\frac{3}{2}\cos\theta_{K_1}\sin\theta_{^1P_1}$	0	$\frac{3}{2}\sin\theta_{K_1}\sin\theta_{^1P_1}$
b_1K		-2	$-\frac{3}{2}\cos\theta_{K_1}$	0	$-\frac{3}{2}\sin\theta_{K_1}$
$K_1(1270)\eta$			0	$\frac{3}{2}\cos\theta_{K_1}\cos\theta_{^1P_1}$	0
$h_1(1415)K$				0	$\frac{3}{2}\sin\theta_{K_1}\cos\theta_{^1P_1}$
$K_1(1400)\eta$					0

Before proceeding, let us discuss the $A_1\phi^8 \to B_1\phi^8$ transitions, with A_1 and B_1 the two SU(3) octets of axial-vector mesons and ϕ^8 the octet of the pseudo-Nambu–Goldstone bosons. Let $A_{1\mu}$ and $B_{1\mu}$ denote the fields for the 1^{++} and 1^{+-} axial-vector meson multiplets, respectively. Under parity transformation, we have $A_{1\mu} \to -A_1^\mu$ and $B_{1\mu} \to -B_1^\mu$; under charge conjugation, we have $A_{1\mu} \to A_{1\mu}^T$ and $B_{1\mu} \to -B_{1\mu}^T$. Then the $A_1\phi^8 \to B_1\phi^8$

transitions can only arise at $\mathcal{O}(p^2)$ with p the momentum scale in the chiral power counting. They are given by operators, such as

$$\langle A_{1\mu}[B_{1\nu},[u^\mu,u^\nu]]\rangle, \tag{17}$$

with

$$u_\mu = i\left(u^\dagger\partial_\mu u - u\partial_\mu u^\dagger\right). \tag{18}$$

Such terms are one order higher in the chiral power counting than the WT terms describing the $A_1\phi^8 \to A_1\phi^8$ and $B_1\phi^8 \to B_1\phi^8$ transitions, and thus will be neglected.

2.2. Unitarization Procedure

The unitarization procedure we adopt follows ChUA in which the scattering amplitudes in Equation (16) are the elements of a matrix, denoted by V, such that it enters as an input to solve the Bethe–Salpeter equation, which in its on-shell factorization form, reads [23]

$$T = (1 - V\,G)^{-1}\,V\,. \tag{19}$$

The V matrix describes the transition between the channels listed in Tables 1–4. In addition, G is the diagonal loop function matrix whose diagonal matrix elements are given by

$$G_l = i\int \frac{d^4q}{(2\pi)^4}\frac{1}{q^2 - m_l^2 + i\epsilon}\frac{1}{(q-P)^2 - M_l^2 + i\epsilon}\,, \tag{20}$$

with m_l and M_l the masses of the pseudoscalar and axial-vector mesons, respectively, involved in the loop in the channel l, and P the total four-momentum of those mesons ($P^2 = s$). After the integration over the temporal component q^0, Equation (20) becomes

$$G_l(s) = \int \frac{d^3q}{(2\pi)^3}\frac{\omega_1+\omega_2}{2\omega_1\omega_2}\frac{1}{(P^0)^2 - (\omega_1+\omega_2)^2 + i\epsilon}\,, \tag{21}$$

with $\omega_1 = \sqrt{{M_l}^2 + |\vec{q}|^2}$ and $\omega_2 = \sqrt{{m_l}^2 + |\vec{q}|^2}$, and can be regularized by means of a cut-off in the three-momentum $q_{\max}$. On the other hand, the function G_l can also be regularized using a subtraction constant as [40]

$$\begin{aligned} G_l^{\mathrm{DR}}(s) = &\frac{1}{16\pi^2}\left[\alpha_l(\mu) + \log\frac{M_l^2}{\mu^2} + \frac{m_l^2 - M_l^2 + s}{2s}\log\frac{m_l^2}{M_l^2} + \frac{p_l}{\sqrt{s}}\left(\log\frac{s - m_l^2 + M_l^2 + 2p_l\sqrt{s}}{-s + m_l^2 - M_l^2 + 2p_l\sqrt{s}}\right.\right. \\ &\left.\left. + \log\frac{s + m_l^2 - M_l^2 + 2p_l\sqrt{s}}{-s - m_l^2 + M_l^2 + 2p_l\sqrt{s}}\right)\right], \end{aligned} \tag{22}$$

where p_l is the three-momentum of the mesons in the center-of-mass (c.m.) frame

$$p_l = \frac{\sqrt{\left(s - (M_l + m_l)^2\right)\left(s - (M_l - m_l)^2\right)}}{2\sqrt{s}}\,, \tag{23}$$

while μ is an arbitrary scale of the regularization. Any changes in the μ scale can be absorbed by the subtraction constant $\alpha_l(\mu)$ such that the result is independent of the scale. We may determine the subtraction constant for each intermediate state of the scattering problem by comparing Equations (21), regularized using $q_{\max}$, and (22) at the threshold. The equivalence between the two prescriptions for the loop-function is discussed in, e.g., Refs. [41–43]. In this work, we follow Ref. [44] and set $\mu = 1$ GeV and $\alpha = -1.35$, which is obtained by matching to hard cut-off regularization with $q_{\max} \simeq 0.7$ GeV in the $f_1(1285)\eta$ channel. This set of parameters are used for all channels, and a variation of the cut-off within $q_{\max} = (0.7 \pm 0.1)$ GeV, and correspondingly $\alpha(\mu = 1\,\mathrm{GeV}) = -1.35 \pm 0.17$, will be used to show the dependence of the results on this parameter.

2.3. Searching for Poles

We move on to the complex energy plane to search for poles in the T-matrix. Specifically, for a single-channel problem, there are two Riemann sheets for the complex energy plane. Bound states show up as poles, below the threshold, in the transition matrix on the real energy axis on the first Riemann sheet, while virtual states manifest themselves below the threshold on the real axis on the second Riemann sheet, and resonances correspond to poles off the real axis on the second Riemann sheet. The Riemann sheets come about because the G loop function has a cut extending from the threshold to infinity which is usually chosen to be along the positive real axis. For n coupled channels, there are n cuts and thus 2^n Riemann sheets. From unitarity and the Schwarz reflection principle, the discontinuity of the G_l function can be read off from its imaginary part,

$$\mathrm{Im}\, G_l(s) = -\frac{p_l}{8\pi\sqrt{s}}\,, \tag{24}$$

which we can use to perform an analytic continuation to the entire complex plane. In this case, the G_l loop function on the "second" Riemann sheet with respect to the lth channel reads

$$G_l^{\mathrm{II}}(s) = G_l^{\mathrm{I}}(s) + i\,\frac{p_l}{4\pi\sqrt{s}}\,; \tag{25}$$

the lower half plane of this Riemann sheet is directly connected to the physical region when the lth channel is open, i.e., $\mathrm{Re}(\sqrt{s}) \geq m + M$. We will label the Riemann sheets according to the sign of the imaginary part of the corresponding c.m. momentum for each channel (see the next section).

Furthermore, it is also possible to determine the pole couplings to the lth channel. Note that close to the pole singularity the T-matrix elements $T_{ij}(s)$ admit a Laurent expansion,

$$T_{ij}(s) = \frac{g_i\, g_j}{s - z_p} + \text{regular terms}, \tag{26}$$

where $z_p = (M_p - i\Gamma/2)^2$ is the pole location on the complex energy plane, with M_p and Γ standing for the pole mass and width, respectively. Therefore, the product of couplings $g_i g_j$ is the residue at the pole in $T_{ij}(s)$ which takes values on the Riemann sheet where the pole is located. In this way, the couplings can be evaluated straightforwardly. For instance, for a diagonal transition it is given by

$$\begin{aligned} g_i^2 &= \frac{r}{2\pi}\int_0^{2\pi} T_{ii}(z(\theta))e^{i\theta}d\theta \\ &= \lim_{s\to z_p}(s - z_p)T_{ii}(s) = \left[\frac{d}{ds}\frac{1}{T_{ii}(s)}\right]^{-1}_{s=z_p}, \end{aligned} \tag{27}$$

where $z(\theta) = z_p + re^{i\theta}$ with r the radius of contour for the integral, and the two lines give two equivalent ways of computing residues.

3. $\eta_1(1855)$ and Its Decays

3.1. Dynamical Generation of the $\eta_1(1855)$

Following the unitarization procedure described previously, we seek dynamically generated states stemming from the S-wave interactions between pseudoscalar and axial-vector mesons. For the $I = 0$ case, the transition amplitudes among the channels listed in Table 1 are determined using Equation (16) with the C_{ij} coefficients given in Table 6. In Table 10, we show the isoscalar poles with exotic quantum numbers $J^{PC} = 1^{-+}$ obtained by solving Equation (19) using those coefficients as well as each set of mixing angles listed in Table 5. We also show the couplings of these poles to the channels spanning the space of states in Table 1.

Table 10. The poles (in GeV) and their corresponding couplings (in GeV) to the channels contributing to the *PA* interaction with $I = 0$ and exotic quantum numbers $J^{PC} = 1^{-+}$. The corresponding Riemann sheet for each pole is listed below the pole position. The dominantly coupled channel is emphasized in boldface for each pole. The errors of the poles are from varying the subtraction constant within $\alpha(\mu = 1\,\text{GeV}) = -1.35 \pm 0.17$, and only the central values of the couplings are given. For each pole, we also give the central values of the peak mass and width as $(M_{\text{peak}}, \Gamma_{\text{peak}})$, after considering the axial-vector meson widths, in the last row of the corresponding panel.

Poles (Set A)		**Channels**			
$\mathbf{1.39 \pm 0.01 - i(0.04 \pm 0.01)}$	$a_1\pi$	$K_1(1270)\bar{K}$	$f_1(1285)\eta$	$K_1(1400)\bar{K}$	$f_1(1420)\eta$
$(-++++)$					
g_l	$\mathbf{5.21 + i3.01}$	$1.22 + i0.78$	$0.01 + i0.02$	$0.36 + i0.35$	0.00
(1.39, 0.24)					
$\mathbf{1.69 \pm 0.03}$	$a_1\pi$	$K_1(1270)\bar{K}$	$f_1(1285)\eta$	$K_1(1400)\bar{K}$	$f_1(1420)\eta$
$(-++++)$					
g_l	$0.36 + i0.98$	$\mathbf{8.16 - i0.17}$	$3.64 + i0.01$	$0.09 - i0.15$	$2.46 + i0.01$
(1.69, 0.08)					
$\mathbf{1.84 \pm 0.03}$	$a_1\pi$	$K_1(1270)\bar{K}$	$f_1(1285)\eta$	$K_1(1400)\bar{K}$	$f_1(1420)\eta$
$(----++)$					
g_l	$0.07 + i0.28$	$0.69 + i0.55$	$1.68 + i0.08$	$\mathbf{9.33 + i0.15}$	$1.16 + i0.06$
(1.84, 0.16)					
Poles (Set B)		**Channels**			
$\mathbf{1.39 \pm 0.01 - i(0.04 \pm 0.01)}$	$a_1\pi$	$K_1(1270)\bar{K}$	$f_1(1285)\eta$	$K_1(1400)\bar{K}$	$f_1(1420)\eta$
$(-++++)$					
g_l	$\mathbf{5.21 + i3.03}$	$0.81 + i0.53$	0.00	$0.55 + i0.54$	0.00
(1.42, 0.34)					
$\mathbf{1.70 \pm 0.02}$	$a_1\pi$	$K_1(1270)\bar{K}$	$f_1(1285)\eta$	$K_1(1400)\bar{K}$	$f_1(1420)\eta$
$(-++++)$					
g_l	$0.25 + i0.67$	$\mathbf{8.34 - i0.08}$	$1.27 - i0.01$	$0.37 + i0.17$	$2.58 - i0.01$
(1.70, 0.10)					
$\mathbf{1.84 \pm 0.03}$	$a_1\pi$	$K_1(1270)\bar{K}$	$f_1(1285)\eta$	$K_1(1400)\bar{K}$	$f_1(1420)\eta$
$(----++)$					
g_l	$0.15 + i0.62$	$0.33 - i0.27$	$1.83 + i0.09$	$\mathbf{9.05 + i0.17}$	$3.81 - i0.20$
(1.85, 0.18)					

Furthermore, in Table 10 we also highlight the Riemann sheets, the first and the second one for each channel, denoted by the $+$ and $-$ signs, respectively. We obtain three poles such that their locations are barely affected by the change of the mixing angles from set A to set B listed in Table 5. The lower pole is at 1.39 GeV with a width of about 0.04 GeV, which is above the $a_1\pi$ threshold. In particular, this channel is open for decay, and the fact that it is this channel the one for which the pole couples mostly, as pointed out in Table 10, explains why that pole has such a value for its width. By contrast, although the $a_1\pi$ channel is also open for decay, the pole at 1.69 GeV has a much smaller width because its coupling to this channel is small compared to the one for $K_1(1400)\bar{K}$, which is the dominant channel for that pole. Similarly, the highest pole, located at 1.84 GeV, couples mostly to the $K_1(1400)\bar{K}$ channel, and has a small imaginary part. In addition, we can also understand why the highest pole couples more to the $K_1(1400)\bar{K}$ than to the $f_1(1285)\eta$. The latter channel is closer to the pole than the former, but from Table 6, the diagonal $f_1(1285)\eta$ transition is not allowed since its WT term is zero. Nevertheless, the pole couples to $f_1(1285)\eta$ through the non-diagonal $K_1(1400)\bar{K}$–$f_1(1285)\eta$ transition, which leads to a small coupling.

3.2. Effects of the Widths of the Axial-Vector Mesons

So far we have neglected the nonzero widths of the axial-vector mesons. In order to investigate their effects on the results, we use complex masses for the intermediate

resonances, that is, $M_i \to M_i - i\Gamma_i/2$. However, by doing that, the analytic properties are lost such that the poles of the T matrix do not correspond to the masses and widths of the obtained resonances any more. On the other hand, we can see the impact of such non-zero widths on the lineshapes of the transition matrix elements.

In Figure 1, we show a comparison between the lineshape for the T-matrix element corresponding to the elastic transition $T_{K_1(1400)\bar{K}\to K_1(1400)\bar{K}}$ with and without including the widths for the intermediate particles. This channel has the strongest coupling to the pole at 1.84 GeV; therefore, we expect that any non-trivial structure should manifest most in its associated T-matrix element. The dashed and solid lines are the $T_{K_1(1400)\bar{K}\to K_1(1400)\bar{K}}$ with zero and non-zero width, respectively, for both sets A and B of mixing angles in Table 1. Notice that, for the case of zero width approximation, the $T_{K_1(1400)\bar{K}\to K_1(1400)\bar{K}}$ lineshape has narrow peaks around 1845 MeV, right at the range of energy where we expect the $\eta_1(1855)$ manifests in our model. The inclusion of finite widths for the axial-vector mesons changes the sharp peak to a broad bump with a width of about 0.2 GeV, which is around the width of the $K_1(1400)$ [10]. Notice that the width matches nicely that of the $\eta_1(1855)$ measured by BESIII, $\left(188 \pm 18^{+3}_{-8}\right)$MeV [8]. One can obtain a peak mass M_{peak} and a peak width Γ_{peak}, defined as the width at the half maximum of the line shape of the diagonal T-matrix element modulus squared for the dominant channel. In Table 10, we also list the values of M_{peak} and Γ_{peak} for each pole. The values for the highest η_1 pole in the table agree remarkably well with those of the $\eta_1(1855)$. These values may be compared with the resonance parameters extracted using the Breit–Wigner form in experimental analyses.

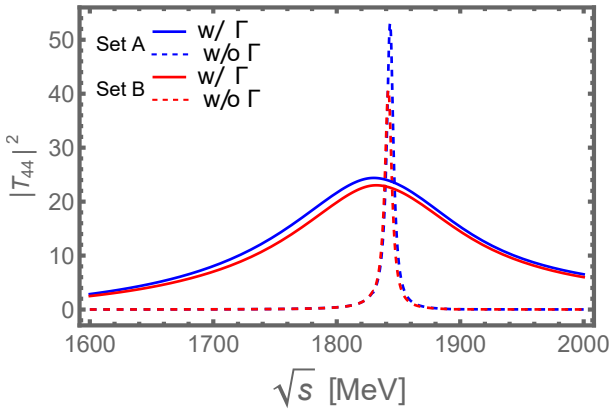

Figure 1. The blue dashed and solid lines are, respectively, the modulus squared of the T-matrix element, corresponding to the diagonal $K_1(1400)\bar{K} \to K_1(1400)\bar{K}$ transition, evaluated with and without the inclusion of the widths associated with the axial-vector mesons taking part in the loop function G_l (Equation (20)).

The results presented may be improved by considering one additional possible contribution due to the axial-meson decays, shown in Figure 2. Since the intermediate vector and pseudoscalar mesons in the triangle diagrams can go on shell, such contributions could further increase the widths of the dynamically generated states. In the following, we will continue to present predictions neglecting the width effects of the axial-vector mesons.

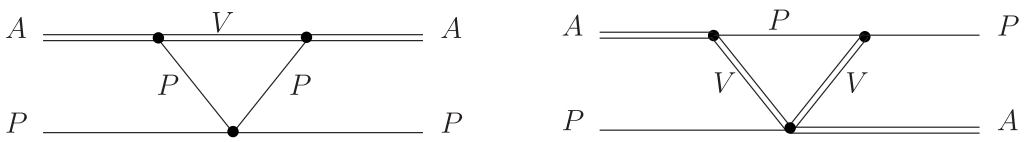

Figure 2. Possible triangle diagram contributions to the scattering between an axial vector meson and a pseudoscalar meson.

Let us briefly discuss the other two predicted isoscalar exotic η_1 mesons in Table 10. The one with a mass of about 1.39 GeV, denoted as $\eta_1(1400)$, is expected to be rather broad

due to the large width of the $a_1(1260)$ as it couples most strongly to the $a_1\pi$ channel. It can be searched for in final states, such as $\rho\pi\pi$ and $K\bar{K}\pi\pi$. The one with a mass around 1.7 GeV, denoted as $\eta_1(1700)$, couples most strongly to the $K_1(1270)\bar{K}$ and is expected to have a width similar to that of the $K_1(1270)$, i.e., around 0.1 GeV. It can also be searched for in final states of $K\bar{K}\pi\pi$.

3.3. The $\eta_1(1855) \to \eta'\eta$ and $K^*\bar{K}\pi$ Decays

Let us first discuss the $\eta_1 \to \eta\eta'$ decay, whose Feynman diagram is shown in Figure 3. Within our approach the $\eta_1(1855)$ structure decays via its $K_1(1400)\bar{K}$ component, with the corresponding coupling constant listed in Table 10. We also need to evaluate the $K_1(1400)\bar{K} \to \eta\eta'$ transition, for which we use the resonance chiral theory (RχT) operators given in Ref. [45].

The RχT operators can be divided regarding the intrinsic-parity sector to which they contribute. Due to its nature, the odd-intrinsic parity sector will contain a Levi–Civita tensor [46–48]; for the $\eta_1 \to \eta\eta'$ decay one cannot saturate the Lorentz indices in such tensor to obtain a non-zero contribution. Thus, only the even-intrinsic parity operators must give a non-vanishing contribution. Since the chiral $\mathcal{O}(p^2)$ Lagrangian does not contribute to such processes [49], we will use the $\mathcal{O}(p^4)$ Lagrangian given in Ref. [45]. From these operators, only three will contribute to this decay. To obtain the largest possible contribution from such operators, we use the upper bounds imposed from chiral counting as performed in Ref. [50]. This amounts to making equal the three coupling constants and setting them to $\lambda_1^A = \lambda_2^A = \lambda_3^A = g = 0.025\ \text{GeV}^{-1}$, which gives a Lagrangian

$$\mathcal{L} = g\Big[\langle A_{\mu\nu}(u^\mu u_\alpha h^{\nu\alpha} + h^{\nu\alpha}u_\alpha u^\mu)\rangle + \langle A_{\mu\nu}(u_\alpha u^\mu h^{\nu\alpha} + h^{\nu\alpha}u^\mu u_\alpha)\rangle + \langle A_{\mu\nu}(u^\mu h^{\nu\alpha}u_\alpha + u_\alpha h^{\nu\alpha}u^\mu)\rangle\Big], \tag{28}$$

where u_μ has been given in Equation (18), $h^{\mu\nu} = \mathcal{D}^{\{\mu}u^{\nu\}}$ is the symmetrized covariant derivative of u_μ and the spin-1 resonance field is given in the antisymmetric tensor formalism [37]. However, since the $\eta_1 \to K_1\bar{K}$ transition is given in terms of Proca fields, we need to express the K_1 as a Proca field. Following Ref. [49], the antisymmetric tensor field can be expressed in terms of the Proca one as follows,

$$R_\mu = \frac{1}{M_R}\partial^\nu R_{\nu\mu}, \tag{29}$$

where M_R is the mass of the resonance. Using the Lagrangian of Equation (28) and expressing the axial resonance in the Proca representation, we obtain the $\eta_1 \to \eta\eta'$ decay amplitude

$$\mathcal{M}_{\eta_1\to\eta\eta'} = -\frac{4m_{\eta_1}^2}{3F_\pi^3 m_{K_1}} g g_{K_1(1400)\bar{K}} G_{K_1\bar{K}}\left[\left(\alpha p_{\eta'}^2 + \frac{1}{\sqrt{2}}\beta p_\eta^2\right)\varepsilon_{\eta_1}\cdot p_\eta + \left(p_\eta \leftrightarrow p_{\eta'}\right)\right], \tag{30}$$

where F_π is the pion decay constant, $g_{K_1\bar{K}}$ is the coupling constant of the pole to the $K_1(1400)\bar{K}$ channel, $G_{K_1\bar{K}}$ is the loop function for the K_1 and $\bar{K}$ mesons, ε_{η_1} is the η_1 vector polarization, and $p_{\eta^{(\prime)}}$ is the momentum of the $\eta^{(\prime)}$. Here, α and β are given in terms of the η-η' mixing angle

$$\alpha = \cos 2\theta_P + 2\sqrt{2}\sin 2\theta_P, \tag{31a}$$

$$\beta = 2\sqrt{2}\cos 2\theta_P - \sin 2\theta_P. \tag{31b}$$

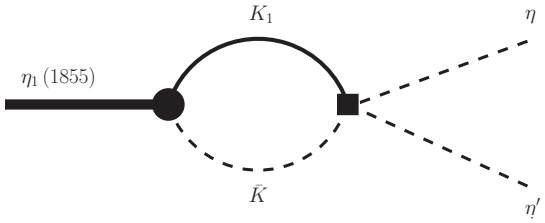

Figure 3. Diagram corresponding to the $\eta_1 \to \eta\eta'$ decay through the $K_1\bar{K}$ loop.

Although one might try to rely in a much simpler way to describe the direct coupling of one axial-vector and three pseudoscalar fields by means of the hidden local symmetry (HLS) Lagrangian [51–53], it is worth to notice that nonetheless, the total amplitude for this process given by the HLS Lagrangian vanishes, which coincides with Equation (30) in the chiral limit.

The decay of η_1 state into $\eta\eta'$ is given by

$$\Gamma_{2B} = \frac{1}{2J+1}\frac{1}{8\pi M_{\eta_1}^2}\left|\mathcal{M}_{\eta_1\to\eta\eta'}\right|^2 q\,, \tag{32}$$

with the amplitude $\mathcal{M}_{\eta_1\to\eta\eta'}$ in Equation (30), while J stands for the η_1 spin. In addition to that, q reads

$$q = \frac{1}{2M_{\eta_1}}\lambda^{1/2}\left(M_{\eta_1}^2, m_{\eta'}^2, m_{\eta}^2\right), \tag{33}$$

with M_{η_1}, $m_{\eta'}$, and m_η the masses for the $\eta_1(1855)$, η', and η mesons, respectively, where $\lambda(x,y,z) = x^2+y^2+z^2-2xy-2yz-2zx$ is the Källén triangle function. Therefore, we obtain the following results for the decay width in this channel

$$\Gamma_{2B} = \begin{cases} (19\pm 4)\,\text{MeV (set A)}\,, \\ (7\pm 2)\,\text{MeV (set B)}\,, \end{cases} \tag{34}$$

where the error is from choosing subtraction constant to be in the range $\alpha(\mu = 1\text{GeV}) = -1.35\pm 0.17$, corresponding to the hard cut-off $q_{\max} = (0.7\pm 0.1)$ GeV as discussed at the end of Section 2.2. For set A, our result agrees with that of Ref. [21], where the $\eta_1(1855)$ was assumed to be a $K_1\bar{K}$ molecule and the same θ_{K_1} mixing angle was used for accounting for the K_{1A} and K_{1B} mixture contributing to the physical $K_1(1270)$ and $K_1(1400)$ states.

As for the $\eta_1 \to \bar{K}K^*\pi$ three-body decay, Figure 4 shows the Feynman diagrams contributing to this process. In particular, the $\eta_1(1855)$ decays through its molecular components, that in our approach are the $K_1(1270)\bar{K}$ and $K_1(1400)\bar{K}$. In this case, the contribution from the $K_1(1270)\bar{K}$ component can be ignored for the following reasons: (1) from Table 10, we see that the relative coupling strength for the $K_1(1270)\bar{K}$ channel is much smaller than that for the $K_1(1400)\bar{K}$ one; (2) the branching ratio $\mathcal{B}[K_1(1270)\to K^*\pi]$ is only 16%, while 96% of the $K_1(1400)$ decays is dominated by the $K^*\pi$. Therefore, from Figure 4 the $\eta_1(1855)\to\bar{K}K^*\pi$ amplitude is written as

$$\mathcal{M}_{3B} = g_{K_1(1400)\bar{K}}\left(-g_{\mu\nu}+\frac{p_\mu p_\nu}{M_{K_1}^2}\right)\frac{1}{p^2-M_{K_1}^2+i\,M_{K_1}\Gamma_{K_1}}\,g_{K^*\pi}\,\varepsilon_{\eta_1}^{\mu}\varepsilon_{K^*}^{\nu}\,, \tag{35}$$

where $g_{K_1(1400)\bar{K}}$ is the coupling of the pole associated with the η_1 state to the $K_1(1400)\bar{K}$ channel, $g_{K^*\pi}$ is the $K_1(1400)K^*\pi$ coupling extracted from the $K_1(1400)\to K^*\pi$ reaction in the Review of Particle Physics (RPP) [10], and $\varepsilon_{\eta_1}^{\mu}$ and $\varepsilon_{K^*}^{\nu}$ are the polarization vectors of the η_1 and K^* mesons, respectively.

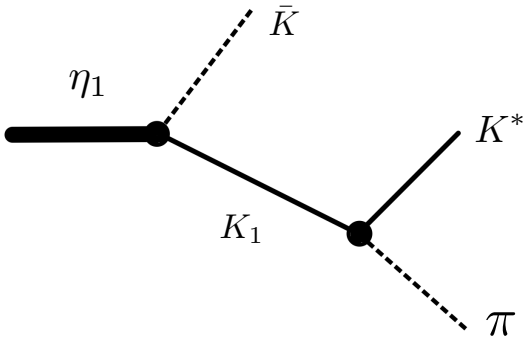

Figure 4. Feynman diagram associated with the three-body decay of the pole through its main component $K_1\bar{K}$.

The differential decay width for the $\eta_1 \to \bar{K}K^*\pi$ process is given by

$$\frac{d\Gamma}{dM_{K_1\bar{K}}} = \frac{1}{(2\pi)^3}\frac{p_K\,\tilde{p_\pi}}{4M_{\eta_1}^2}\,|\mathcal{M}_{3B}|^2\,\frac{1}{2J+1}\,, \tag{36}$$

where

$$\tilde{p}_\pi = \frac{1}{2M_{K_1}}\,\lambda^{1/2}\left(M_{K_1}^2, m_{K^*}^2, m_\pi^2\right), \tag{37}$$

and

$$p_K = \frac{1}{2M_{\eta_1}}\,\lambda^{1/2}\left(M_{\eta_1}^2, m_K^2, M_{K_1}^2\right), \tag{38}$$

with M_{K_1}, m_{K^*}, m_π being the masses of the $K_1(1400)$, K^* and π mesons.

From Equation (36) we obtain the following results for the $\eta_1 \to \bar{K}K^*\pi$ decay width

$$\begin{aligned}\Gamma_{3B} &= \left(81^{+11}_{-24}\,\text{MeV}\right)^A,\\ \Gamma_{3B} &= \left(74^{+12}_{-24}\,\text{MeV}\right)^B,\end{aligned} \tag{39}$$

where the uncertainties come from the subtraction constant (cut-off) used to regularize the loops in Equation (22) (Equation (21)). As can be seen from Equation (39), we obtain similar results whether we use the sets A or B. For the sake of comparison to other works, we evaluate the ratio Γ_{2B}/Γ_{3B}, and obtain

$$\frac{\Gamma_{2B}}{\Gamma_{3B}} = \left(0.23^{-0.08}_{+0.16}\right)^A \text{ or } \left(0.10^{-0.03}_{+0.08}\right)^B, \tag{40}$$

which is consistent to the results in Ref. [21], where the η_1 is also assumed to be a $K_1(1400)\bar{K}$ molecular state. On the other hand, adopting the same multiquark configuration than the present work and Ref. [21], the authors of Ref. [22] have found a different result for the ratio, $\Gamma_{2B}/\Gamma_{3B} \approx 0.03$. Nevertheless, in all the cases the results point out that the $\bar{K}K^*\pi$ three-body channel is more likely than the $\eta\eta'$ one.

4. The $\pi_1(1400/1600)$ Dynamical Generation

The WT amplitudes for the pseudoscalar-axial vector meson interactions with $I = 1$ are given by Equation (16), with the corresponding C_{ij} coefficients listed in Table 7. In this case, from Equation (19), we obtain two π_1 poles shown in Table 11.

Table 11. Poles and their corresponding couplings to the channels contributing to the *PA* interaction with $J^{PC} = 1^{-+}$ and $I = 1$. The dominantly coupled channel is emphasized in boldface for each pole. The errors of the poles are from varying the subtraction constant within $\alpha(\mu = 1\,\text{GeV}) = -1.35 \pm 0.17$, and only the central values of the couplings are given. The last row of each panel gives the central values of the peak mass and width $(M_{\text{peak}}, \Gamma_{\text{peak}})$ for the corresponding pole after considering the axial-vector meson widths.

Poles (Set A)			**Channels**			
$\mathbf{1.47 \pm 0.01 - i(0.12 \pm 0.02)}$	$b_1\pi$	$f_1(1285)\pi$	$f_1(1420)\pi$	$K_1(1270)\bar{K}$	$a_1\eta$	$K_1(1400)\bar{K}$
$(--+++)$						
g_l	$\mathbf{5.22 + i4.40}$	$0.02 - i0.09$	$0.03 - i0.05$	$1.25 + i1.27$	$0.02 - i0.12$	$1.33 + i1.63$
(1.56, 0.46)						
$\mathbf{1.75 \pm 0.02 - i(0.02 \pm 0.01)}$	$b_1\pi$	$f_1(1285)\pi$	$f_1(1420)\pi$	$K_1(1270)\bar{K}$	$a_1\eta$	$K_1(1400)\bar{K}$
$(---++)$						
g_l	$0.10 + i0.95$	$2.73 - i0.02$	1.89	$\mathbf{5.84 - i1.85}$	$3.49 - i0.03$	$2.65 - i0.53$
(1.74, 0.30)						
Poles (Set B)			**Channels**			
$\mathbf{1.47 \pm 0.01 - i(0.12 \pm 0.02)}$	$b_1\pi$	$f_1(1285)\pi$	$f_1(1420)\pi$	$K_1(1270)\bar{K}$	$a_1\eta$	$K_1(1400)\bar{K}$
$(--+++)$						
g_l	$\mathbf{5.27 + i4.31}$	$0.01 - i0.03$	$0.03 - i0.06$	$1.97 - i1.81$	$0.02 - i0.08$	$0.91 + i1.07$
(1.57, 0.50)						
$\mathbf{1.77 \pm 0.01 - i(0.01 \pm 0.01)}$	$b_1\pi$	$f_1(1285)\pi$	$f_1(1420)\pi$	$K_1(1270)\bar{K}$	$a_1\eta$	$K_1(1400)\bar{K}$
$(---++)$						
g_l	$0.13 + i1.44$	$1.37 - i0.25$	$2.86 - i0.50$	$\mathbf{4.80 - i2.29}$	$3.53 - i0.64$	$4.54 - i1.77$
(1.72, 0.20)						

Similar to the previous section, we also provide the couplings of these dynamically generated states to the channels listed in Table 2. Table 11 shows a broad π_1 pole at 1.47 GeV, and a width of about 0.12 GeV.[1] This state is above the $b_1\pi$ and $f_1(1285)\pi$ thresholds. Its large width stems from the large coupling to the $b_1\pi$ and the fact that this channel is open for decaying. The $f_1(1285)\pi$ channel is also open. However, according to Table 7, the corresponding WT term in Equation (16) is zero for the diagonal $f_1(1285)\pi$ transition. On the other hand, the next π_1 pole in Table 11 has a sizeable dependence on the mixing angles. Using set *A*, we find that pole at 1.75 GeV. It couples most strongly to the $K_1(1270)\bar{K}$ channel, which is closed for decaying. Nonetheless, the state can decay into $b_1\pi$ and $f_1(1285)\pi$, albeit their corresponding couplings are small compared to the $K_1(1270)\bar{K}$ one, but still large enough to provide a sizeable width for the pole. In contrast, when set *B* is adopted, the higher π_1 pole is now located at 1.77 GeV, above the $f_1(1420)\pi$ threshold, which is now open. One might think that the width should increase since now three channels are open for decaying. However, although the coupling to the $f_1(1420)\pi$ has increased in this case, at the same time the couplings to the other open channels have decreased. Hence, the overall effect leads to a smaller width compared to the previous case.

The lower pole mass is slightly higher than the mass of the $\pi_1(1400)$ state listed in RPP, (1354 ± 25) MeV [10]. Notice that we use the same subtraction constant for all channels. In principle, it can take different values and lead to a shift of the poles. In addition, we did not include in the loops the b_1 width, that is relatively large and whose effects could influence the pole position. However, it is expected to affect more the imaginary part of the pole than the real one (see Figure 5a below). We can obtain a rough estimate of this change by adding the b_1 width to the previous result for $\text{Im}(z_1)$, with z_1 the lower π_1 pole, i.e.,

$$\Gamma_{b_1} + 2\text{Im}(z_1) \approx 0.4\ \text{GeV}\,, \tag{41}$$

which is close to the $\pi_1(1400)$ width reported in RPP, (330 ± 35) MeV [10]. From these results, we are led to claim that the lower π_1 pole may explain the $\pi_1(1400)$ resonance; in

other words, the $\pi_1(1400)$ is suitably described in our approach as a dynamically generated state with the $b_1\pi$ as its main component.

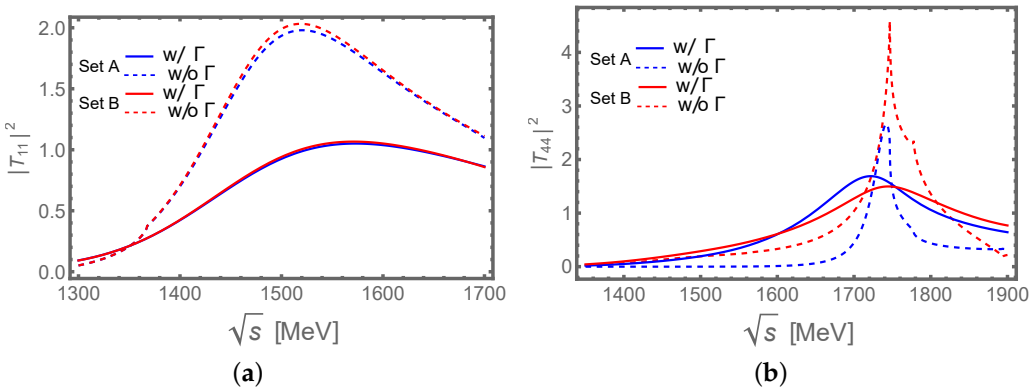

Figure 5. The dashed and solid lines correspond to zero and full widths of the axial-vector mesons in G^{Cut}. (**a**) Modulus square of elastic $b_1\pi$ scattering; (**b**) Modulus square of elastic $K_1(1270)\bar{K}$ scattering.

Alternatively, following the prescription used in Section 3, we can also study the changes in the results caused by the inclusion of the finite widths for the axial-vector mesons by looking at the line shape for the relevant T-matrix elements. In Figure 5a, we show the line shapes for the T-matrix element corresponding to the elastic $b_1\pi \to b_1\pi$ transition, which is the one we would expect the lower pole in Table 11 manifests most due to its large coupling to the $b_1\pi$ channel. It becomes clear that the bumps become broader when the widths of axial-vector mesons are taken into account. A similar behavior can be seen in Figure 5b for the T-matrix element associated with the scattering of $K_1(1270)\bar{K}$, which is the channel to which the higher π_1 pole couples most strongly. The peak mass and width extracted from the line shape of the diagonal T-matrix element for the dominantly coupled channel are also listed in Table 11 when the axial-vector meson widths are considered.

The higher π_1 pole, denoted now by z_2, has a mass consistent with that of the $\pi_1(1600)$, whose pole mass has been reported to be $\left(1623 \pm 47^{+24}_{-75}\right)$ MeV in Ref. [54] and $(1564 \pm 24 \pm 86)$ MeV in Ref. [55]. It can decay into the $\eta'\pi$ and $f_1(1285)\pi$ channels. The corresponding diagrams for both amplitudes are illustrated in Figure 6, from which we have

$$\mathcal{M}_{f_1(1285)\pi} = g_{f_1(1285)\pi}\varepsilon_{\eta_1}\cdot\varepsilon_{f_1}\,, \tag{42}$$

and

$$\mathcal{M}_{\eta'\pi} = g_{K_1\bar{K}}G_{K_1\bar{K}}V_{K_1\bar{K},\eta'\pi}\cdot\varepsilon_{\eta_1} + g_{a_1\eta}G_{a_1\eta}V_{a_1\eta,\eta'\pi}\cdot\varepsilon_{\eta_1}\,, \tag{43}$$

with ε_{η_1} and ε_{f_1} the polarization vectors of the η_1 and $f_1(1285)$ mesons. Here, $g_{f_1(1285)\pi}$, $g_{K_1\bar{K}}$, and $g_{a_1\eta}$ are the effective coupling of the z_2 pole to the corresponding couplings, and $G_{K_1\bar{K}}$ and $G_{a_1\eta}$ are the loops involving the $K_1\bar{K}$ and $a_1\eta$ mesons, respectively. Notice that the effective couplings are computed from the residues of the T matrix elements; thus they contain contributions from all coupled channels.

In order to compare our findings with the experimental information, we evaluate the ratio

$$\mathcal{R}_1 = \frac{|\mathcal{M}_{f_1(1285)\pi}|^2\, q}{|\mathcal{M}_{\eta'\pi}|^2\, \tilde{q}}\,, \tag{44}$$

where q and $\tilde{q}$ are the momentum in the c.m. frame of the $f_1(1285)\pi$ and $\eta'\pi$ pairs, respectively. Numerically, Equation (44) gives

$$\mathcal{R}_1 = \begin{cases} \left(2.4^{+0.8}_{-0.6}\right)^A, \\ \left(2.1^{+0.4}_{-0.3}\right)^B. \end{cases} \tag{45}$$

The ratio is slightly bigger for the mixing angles in the set A. Nevertheless, the result in Equation (45) is consistent to the corresponding ratio 3.80 ± 0.78 reported by the E852 Collaboration [56]. This good agreement with the experimental data supports the molecular picture for the $\pi_1(1600)$ state.

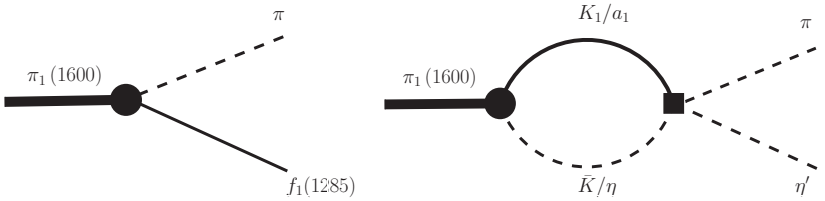

Figure 6. (**a**) Diagram corresponding to the $\pi_1(1600) \to f_1(1285)\pi$ reaction, and (**b**) the $\pi_1(1600) \to \eta'\pi$ decay also via the AP loop. The filled circles represent the effective couplings of the π_1 to the AP meson pairs calculated from the residues. The rectangles are the $AP \to \eta'\pi$ transition amplitudes at tree level.

5. Dynamical Generation in $I = 1/2$ Sector

In the $I = 1/2$ sector, the corresponding WT amplitudes are given by Equation (16) with the C_{ij} coefficients given in Tables 8 and 9. For each case, we have found two poles for parameter sets A and B, as shown in Tables 12 and 13.

Similarly to the previous cases, the poles are located on the same Riemann sheets in both sets of mixing angles. The interactions in the a_1K and b_1K channels are strong to generate a bound state in each of them. The existence of a lower $h_1(1170)K$ channel below the b_1K threshold moves the pole in Table 13 to Riemann sheet $(-+++)$. It has a non-zero imaginary part of a few MeV, which is not shown in the table due to precision.

As discussed before, the $I = 1/2$ poles in Tables 12 and 13 will receive sizeable widths once the width effects of the axial-vector mesons are taken into account, and it is expected that the widths are of the order of a few hundred MeV, like those of the b_1 and a_1 mesons. The peak mass and width for each pole are also listed in the tables when the axial-vector meson widths are considered. Although we neglected the transitions between the A_1P and B_1P sectors as discussed around Equation (17) in Section 2, strange mesons are not C-parity eigenstates and the two dynamically generated $I = 1/2\ 1^-$ states will inevitably mix. The two mixed states together could correspond to the 1^- $K^*(1680)$ structure [10].

Table 12. Poles and their corresponding couplings to the channels contributing to the PA interaction with $J^P = 1^-$. Here the flavor-neutral axial mesons have $J^{PC} = 1^{++}$. The dominantly coupled channel is emphasized in boldface for each pole. The errors of the poles are from varying the subtraction constant within $\alpha(\mu = 1\,\text{GeV}) = -1.35 \pm 0.17$, and only the central values of the couplings are given. The last row of each panel gives the central values of the peak mass and width $(M_{\text{peak}}, \Gamma_{\text{peak}})$ for the corresponding pole after considering the axial-vector meson widths.

Poles (Set A)		**Channels**			
$\mathbf{1.69 \pm 0.02}$	a_1K	$f_1(1285)K$	$K_1(1270)\eta$	$f_1(1420)K$	$K_1(1400)\eta$
$(+++++)$					
g_l	**6.89**	0.89	3.75	0.54	2.10
(1.70, 0.28)					
Poles (Set B)		**Channels**			
$\mathbf{1.70 \pm 0.02}$	a_1K	$f_1(1285)K$	$K_1(1270)\eta$	$f_1(1420)K$	$K_1(1400)\eta$
$(+++++)$					
g_l	**6.58**	0.25	2.45	0.27	3.15
(1.70, 0.30)					

Table 13. Poles and their corresponding couplings to the channels contributing to the *PA* interaction with $J^P = 1^-$. Here the flavor-neutral axial mesons have $J^{PC} = 1^{+-}$. The dominantly coupled channel is emphasized in boldface for each pole. The errors of the poles are from varying the subtraction constant within $\alpha(\mu = 1\,\text{GeV}) = -1.35 \pm 0.17$, and only the central values of the couplings are given. The last row of each panel gives the central values of the peak mass and width $(M_{\text{peak}}, \Gamma_{\text{peak}})$ for the corresponding pole after considering the axial-vector meson widths.

Poles (Set A)		**Channels**			
$\mathbf{1.70 \pm 0.02}$ $(-+++-+)$	$h_1(1170)K$	b_1K	$K_1(1270)\eta$	$h_1(1415)K$	$K_1(1400)\eta$
g_l **(1.70, 0.14)**	0.20	**6.46**	$2.38 - i0.01$	0.50	$3.21 - i0.02$
Poles (Set B)		**Channels**			
$\mathbf{1.69 \pm 0.02}$ $(-+++-+)$	$h_1(1170)K$	b_1K	$K_1(1270)\eta$	$h_1(1415)K$	$K_1(1400)\eta$
g_l **(1.70, 0.14)**	$0.55 - i0.01$	$\mathbf{6.78 + i0.02}$	$3.69 - i0.06$	$0.83 - i0.01$	$2.17 - i0.04$

6. Conclusions

We have studied the interactions between the pseudoscalar and axial-vector mesons in coupled channels with $J^{PC} = 1^{-(+)}$ quantum numbers for the isospin 0, 1, and 1/2 sectors. Using the chiral unitary approach, we describe the interaction with the Weinberg–Tomozawa term derived from chiral Lagrangians. The transition amplitudes among all the relevant channels are unitarized using the Bethe–Salpeter equation from which resonances (bound states) manifest themselves as poles on the (un)physical Riemann sheets of the complex energy plane.

We consider the physical isoscalar axial-vector states as mixtures of the corresponding SU(3) singlets and octets. In addition, the $K_1(1270)$ and $K_1(1400)$ physical states are also mixtures of the K_{1A} and K_{1B} mesons, which are the strange partners of the a_1 and b_1 resonances, respectively. We group into two sets, called A and B, the mixing angles accounting for such mechanisms and investigate their influence on the pole positions.

According to our findings, we obtain poles with $J^{P(C)} = 1^{-(+)}$ quantum numbers in the energy range from 1.30 to 2.00 GeV, in each isospin sector studied ($I = 0, 1, 1/2$). The 1^{-+} quantum numbers are exotic in the sense that they cannot be formed from a pair of quark and antiquark. In particular, we have found an isoscalar state that may correspond to the $\eta_1(1855)$ state, newly observed by the BESIII Collaboration [8]. In addition, we have also found two dynamically generated isovector states that we assign to be the $\pi_1(1400)$ and $\pi_1(1600)$ resonances. Hence, within our formalism, they are dynamically generated through the pseudoscalar-axial vector meson interactions, with the $\eta_1(1855)$ state coupling mostly to $K_1(1400)\bar{K}$ channel, while the $\pi_1(1400)$ couples strongly to the $b_1\pi$, and $\pi_1(1600)$ structure couples most strongly to the $K_1(1270)\bar{K}$. We also find two $I = 1/2$ $J^P = 1^-$ states with a mass around 1.7 GeV. They combined together could be responsible to the observed $K^*(1680)$ structure.

In addition, we also evaluate the decays of the $\eta_1(1855)$ and the $\pi_1(1600)$. We find that the three-body decay channel $\bar{K}K^*\pi$ has a significantly larger branching fraction than the $\eta'\eta$, which is the channel where the observation of the $\eta_1(1855)$ was made. The obtained ratio between the $\pi_1(1600) \to f_1(1285)\pi$ and $\pi_1(1600) \to \eta'\pi$ decays, given by Equation (45), is consistent with the corresponding experimental value.

We suggest searching for two additional η_1 exotic mesons with masses of about 1.4 and 1.7 GeV, respectively. In particular, the latter should be relatively narrow with a width around 0.1 GeV and one of its main decay channels is $K\bar{K}\pi\pi$.

Author Contributions: Methodology: M.-J.Y.; writing—original draft preparation: J.M.D. and A.G.; writing—review and editing: F.-K.G.; supervision: F.-K.G. and B.-S.Z. All authors have read and agreed to the published version of the manuscript.

Funding: This project is supported in part by the National Natural Science Foundation of China (NSFC) under Grants No. 12125507, No. 11835015, and No. 12047503; by the China Postdoctoral Science Foundation under Grant No. 2022M713229; by the NSFC and the Deutsche Forschungsgemeinschaft (DFG) through the funds provided to the Sino-German Collaborative Research Center TRR110 "Symmetries and the Emergence of Structure in QCD" (NSFC Grant No. 12070131001, DFG Project-ID 196253076); and by the Chinese Academy of Sciences under Grant No. XDB34030000.

Acknowledgments: M.J.Y. is grateful to Shuang-Shi Fang and M.P. Valderrama for valuable discussions.

Data Availability Statement: Data available in a publicly accessible repository.

Conflicts of Interest: The authors declare no conflict of interest.

Notes

[1] As discussed in Section 3.2, the widths of the dynamically generated poles will be significantly increased once the width effects of the axial-vector mesons are taken into account, see also the discussions below.

References

1. Chodos, A.; Jaffe, R.L.; Johnson, K.; Thorn, C.B.; Weisskopf, V.F. A New Extended Model of Hadrons. *Phys. Rev. D* **1974**, *9*, 3471–3495. [CrossRef]
2. Jaffe, R.L. Multi-Quark Hadrons. 1. The Phenomenology of (2 Quark 2 anti-Quark) Mesons. *Phys. Rev. D* **1977**, *15*, 267. [CrossRef]
3. Maiani, L.; Piccinini, F.; Polosa, A.D.; Riquer, V. Diquark-antidiquarks with hidden or open charm and the nature of X(3872). *Phys. Rev. D* **2005**, *71*, 014028. [CrossRef]
4. Esposito, A.; Pilloni, A.; Polosa, A.D. Multiquark Resonances. *Phys. Rept.* **2017**, *668*, 1–97. [CrossRef]
5. Guo, F.K.; Hanhart, C.; Meißner, U.G.; Wang, Q.; Zhao, Q.; Zou, B.S. Hadronic molecules. *Rev. Mod. Phys.* **2018**, *90*, 015004. Erratum in *Rev. Mod. Phys.* **2022**, *94*, 029901. [CrossRef]
6. Luo, X.Q.; Liu, Y. Gluonic excitation of non-exotic hybrid charmonium from lattice QCD. *Phys. Rev. D* **2006**, *74*, 034502. Erratum in *Phys. Rev. D* **2006**, *74*, 039902. [CrossRef]
7. Meyer, C.A.; Swanson, E.S. Hybrid Mesons. *Prog. Part. Nucl. Phys.* **2015**, *82*, 21–58. [CrossRef]
8. Ablikim, M.; et al.; [BESIII Collaboration]. Observation of an Isoscalar Resonance with Exotic $J^{PC} = 1^{-+}$ Quantum Numbers in $J/\psi \to \gamma\eta\eta'$. *Phys. Rev. Lett.* **2022**, *129*, 192002. [CrossRef]
9. Ablikim,, M.; et al.; [BESIII Collaboration]. Partial wave analysis of $J/\psi \to \gamma\eta'\eta'$. *Phys. Rev. D* **2022**, *105*, 072002. [CrossRef]
10. Workman, R.L. et al. [Particle Data Group Collaboration]. Review of Particle Physics. *PTEP* **2022**, *2022*, 083C01. [CrossRef]
11. Lacock, P.; Michael, C.; Boyle, P.; Rowland, P. Orbitally excited and hybrid mesons from the lattice. *Phys. Rev. D* **1996**, *54*, 6997–7009. [CrossRef]
12. Lacock, P.; Michael, C.; Boyle, P.; Rowland, P. Hybrid mesons from quenched QCD. *Phys. Lett. B* **1997**, *401*, 308–312. [CrossRef]
13. Bernard, C.; Hetrick, J.E.; DeGrand, T.A.; Wingate, M.; DeTar, C.; McNeile, C.; Gottlieb, S.; Heller, U.M.; Rummukainen, K.; Sugar, B.; et al. Exotic mesons in quenched lattice QCD. *Phys. Rev. D* **1997**, *56*, 7039–7051. [CrossRef]
14. McNeile, C.; Michael, C. Decay width of light quark hybrid meson from the lattice. *Phys. Rev. D* **2006**, *73*, 074506. [CrossRef]
15. Dudek, J.J.; Edwards, R.G.; Peardon, M.J.; Richards, D.G.; Thomas, C.E. Toward the excited meson spectrum of dynamical QCD. *Phys. Rev. D* **2010**, *82*, 034508. [CrossRef]
16. Dudek, J.J. The lightest hybrid meson supermultiplet in QCD. *Phys. Rev. D* **2011**, *84*, 074023. [CrossRef]
17. Qiu, L.; Zhao, Q. Towards the establishment of the light $J^{P(C)} = 1^{-(+)}$ hybrid nonet *. *Chin. Phys. C* **2022**, *46*, 051001. [CrossRef]
18. Shastry, V.; Fischer, C.S.; Giacosa, F. The phenomenology of the exotic hybrid nonet with $\pi_1(1600)$ and $\eta_1(1855)$. *arXiv* **2022**, arXiv:hep-ph/2203.04327.
19. Chen, H.X.; Su, N.; Zhu, S.L. QCD Axial Anomaly Enhances the $\eta\eta'$ Decay of the Hybrid Candidate $\eta_1(1855)$. *Chin. Phys. Lett.* **2022**, *39*, 051201. [CrossRef]
20. Wan, B.D.; Zhang, S.Q.; Qiao, C.F. A possible structure of newly found exotic state $\eta_1(1855)$. *arXiv* **2022**, arXiv:hep-ph/2203.14014.
21. Dong, X.K.; Lin, Y.H.; Zou, B.S. Interpretation of the η_1 (1855) as a $K\bar{K}_1(1400)$ + c.c. molecule. *Sci. China Phys. Mech. Astron.* **2022**, *65*, 261011. [CrossRef]
22. Yang, F.; Zhu, H.Q.; Huang, Y. Analysis of the η_1 (1855) as a $K\bar{K}_1(1400)$molecular state. *Nucl. Phys. A* **2023**, *1030*, 122571. [CrossRef]
23. Oller, J.A.; Oset, E.; Ramos, A. Chiral unitary approach to meson meson and meson - baryon interactions and nuclear applications. *Prog. Part. Nucl. Phys.* **2000**, *45*, 157–242. [CrossRef]
24. Hofmann, J.; Lutz, M.F.M. Open charm meson resonances with negative strangeness. *Nucl. Phys. A* **2004**, *733*, 142–152. [CrossRef]

25. Roca, L.; Oset, E.; Singh, J. Low lying axial-vector mesons as dynamically generated resonances. *Phys. Rev. D* **2005**, *72*, 014002. [CrossRef]
26. Guo, F.K.; Shen, P.N.; Chiang, H.C.; Ping, R.G.; Zou, B.S. Dynamically generated 0^+ heavy mesons in a heavy chiral unitary approach. *Phys. Lett. B* **2006**, *641*, 278–285. [CrossRef]
27. Dias, J.M.; Debastiani, V.R.; Xie, J.J.; Oset, E. Doubly charmed Ξ_{cc} molecular states from meson-baryon interaction. *Phys. Rev. D* **2018**, *98*, 094017. [CrossRef]
28. Guo, F.K.; Meißner, U.G. More kaonic bound states and a comprehensive interpretation of the D_{sJ} states. *Phys. Rev. D* **2011**, *84*, 014013. [CrossRef]
29. Aaij, R.; ABeteta, C.A.; Ackernley, T.; Adeva, B.; Adinolfi, M.; Afsharnia, H.; Aidala, C.A.; Aiola, S.; Ajaltouni, Z.; Akar, S.; et al. Observation of New Resonances Decaying to $J/\psi K^+$ and $J/\psi\phi$. *Phys. Rev. Lett.* **2021**, *127*, 082001. [CrossRef]
30. Cheng, H.Y. Revisiting Axial-Vector Meson Mixing. *Phys. Lett. B* **2012**, *707*, 116–120. [CrossRef]
31. Amsler, C.; Close, F.E. Is $f_0(1500)$ a scalar glueball? *Phys. Rev. D* **1996**, *53*, 295–311. [CrossRef]
32. Meißner, U.G. Low-Energy Hadron Physics from Effective Chiral Lagrangians with Vector Mesons. *Phys. Rept.* **1988**, *161*, 213. [CrossRef]
33. 't Hooft, G. A Planar Diagram Theory for Strong Interactions. *Nucl. Phys. B* **1974**, *72*, 461. [CrossRef]
34. Witten, E. Current Algebra Theorems for the U(1) Goldstone Boson. *Nucl. Phys. B* **1979**, *156*, 269–283. [CrossRef]
35. Veneziano, G. Goldstone Mechanism From Gluon Dynamics. *Phys. Lett. B* **1980**, *95*, 90–92. [CrossRef]
36. Guo, Z.H.; Oller, J.A. Resonances from meson-meson scattering in U(3) CHPT. *Phys. Rev. D* **2011**, *84*, 034005. [CrossRef]
37. Ecker, G.; Gasser, J.; Leutwyler, H.; Pich, A.; de Rafael, E. Chiral Lagrangians for Massive Spin 1 Fields. *Phys. Lett. B* **1989**, *223*, 425–432. [CrossRef]
38. Birse, M.C. Effective chiral Lagrangians for spin 1 mesons. *Z. Phys. A* **1996**, *355*, 231–246. [CrossRef]
39. Borasoy, B.; Meißner, U.G. Chiral Lagrangians for baryons coupled to massive spin 1 fields. *Int. J. Mod. Phys. A* **1996**, *11*, 5183–5202. [CrossRef]
40. Oller, J.A.; Oset, E. N/D description of two meson amplitudes and chiral symmetry. *Phys. Rev. D* **1999**, *60*, 074023. [CrossRef]
41. Oller, J.A.; Oset, E.; Pelaez, J.R. Meson meson interaction in a nonperturbative chiral approach. *Phys. Rev. D* **1999**, *59*, 074001. Erratum in *Phys. Rev. D* **1999**, *60*, 099906; *Phys. Rev. D* **2007**, *75*, 099903. [CrossRef]
42. Oller, J.A.; Meißner, U.G. Chiral dynamics in the presence of bound states: Kaon nucleon interactions revisited. *Phys. Lett. B* **2001**, *500*, 263–272. [CrossRef]
43. Fu, H.L.; Grießhammer, H.W.; Guo, F.K.; Hanhart, C.; Meißner, U.G. Update on strong and radiative decays of the $D^*_{s0}(2317)$ and $D_{s1}(2460)$ and their bottom cousins. *Eur. Phys. J. A* **2022**, *58*, 70. [CrossRef]
44. Geng, L.S.; Oset, E. Vector meson-vector meson interaction in a hidden gauge unitary approach. *Phys. Rev. D* **2009**, *79*, 074009. [CrossRef]
45. Cirigliano, V.; Ecker, G.; Eidemuller, M.; Kaiser, R.; Pich, A.; Portoles, J. Towards a consistent estimate of the chiral low-energy constants. *Nucl. Phys. B* **2006**, *753*, 139–177. [CrossRef]
46. Wess, J.; Zumino, B. Consequences of anomalous Ward identities. *Phys. Lett. B* **1971**, *37*, 95–97. [CrossRef]
47. Witten, E. Global Aspects of Current Algebra. *Nucl. Phys. B* **1983**, *223*, 422–432. [CrossRef]
48. Kampf, K.; Novotny, J. Resonance saturation in the odd-intrinsic parity sector of low-energy QCD. *Phys. Rev. D* **2011**, *84*, 014036. [CrossRef]
49. Ecker, G.; Gasser, J.; Pich, A.; de Rafael, E. The Role of Resonances in Chiral Perturbation Theory. *Nucl. Phys. B* **1989**, *321*, 311–342. [CrossRef]
50. Miranda, J.A.; Roig, P. New τ-based evaluation of the hadronic contribution to the vacuum polarization piece of the muon anomalous magnetic moment. *Phys. Rev. D* **2020**, *102*, 114017. [CrossRef]
51. Bando, M.; Fujiwara, T.; Yamawaki, K. Generalized Hidden Local Symmetry and the A_1 Meson. *Prog. Theor. Phys.* **1988**, *79*, 1140. [CrossRef]
52. Bando, M.; Kugo, T.; Yamawaki, K. Nonlinear Realization and Hidden Local Symmetries. *Phys. Rept.* **1988**, *164*, 217–314. [CrossRef]
53. Kaiser, N.; Meißner, U.G. Generalized hidden symmetry for low-energy hadron physics. *Nucl. Phys. A* **1990**, *519*, 671–696. [CrossRef]
54. Kopf, B.; Albrecht, M.; Koch, H.; Küßner, M.; Pychy, J.; Qin, X.; Wiedner, U. Investigation of the lightest hybrid meson candidate with a coupled-channel analysis of $\bar{p}p$-, π^-p- and $\pi\pi$-Data. *Eur. Phys. J. C* **2021**, *81*, 1056. [CrossRef]
55. Rodas, A.; Pilloni, A.; Albaladejo, M.; Fernández-Ramírez, C.; Jackura, A.; Mathieu, V.; Mikhasenko, M.; Nys, J.; Pauk, V.; Ketzer, B.; et al. Determination of the pole position of the lightest hybrid meson candidate. *Phys. Rev. Lett.* **2019**, *122*, 042002. [CrossRef]
56. Kuhn, J.; et al. [E852 Collaboration]. Exotic meson production in the $f_1(1285)\pi^-$system observed in the reaction $\pi^-p \to \eta\pi^+\pi^-\pi^-p$ at 18GeV/c. *Phys. Lett. B* **2004**, *595*, 109–117. [CrossRef]